**PAPER • OPEN ACCESS**

# Effects of FOD on fatigue strength of 7075-T6 hourglass specimens

To cite this article: E V Arcieri *et al* 2021 *IOP Conf. Ser.: Mater. Sci. Eng.* **1038** 012012

View the article online for updates and enhancements.

# Effects of FOD on fatigue strength of 7075-T6 hourglass specimens

**E V Arcieri**[1], **S Baragetti**[1] **and M Lavella**[1]

[1] Department of Management, Information and Production Engineering, University of Bergamo, Viale Marconi 5, Dalmine 24044, Italy

sergio.baragetti@unibg.it

**Abstract**. The term "Foreign Object Damage (FOD)" refers to the damage associated with the impact of particles on aircraft engine components that causes changes in fatigue strength as a result of induced stress concentrations, residual stresses and microstructural changes. This paper presents the Finite Element (FE) models created to study the stress field induced by the impacts of a steel sphere on a 7075-T6 hourglass specimen. The impacts occur at the minimum cross section, in the normal and oblique directions. The results reveal that in the event of an oblique impact the axial tensile stresses are greater and closer to the crater created by the impact. The superposition of the residual axial stresses to the bending stresses by fatigue test allows to identify the areas in which the maximum stresses are reached and therefore crack initiation is expected.

## 1. Introduction

FOD is the damage induced by the impact of particles on the components of the aircraft engine ingested during take-off, taxiing and landing. These particles can be debris and sand and they could cause craters, nicks and dents which can change the fatigue strength of the component [1-2]. Studies show that essentially four factors affect fatigue strength: (i) generation of micro-cracks; (ii) generation of other microstructural damages such as shear bands and local textures; (iii) stress concentrations; (iv) induced residual stresses.

Often the fatigue life of a part subjected to FOD is influenced by microscopic structural effects. Peters and Ritchie [3] simulated FOD by firing hardened steel spheres in the normal direction to the surface of a specimen using compressed air-gun setup and observed the induced microstructural effects. From their analysis, they drew the important consideration that the nature of the microstructural damage is a function of the impact speed. The impact at high speed (300 m/s) generated pile-up of material at the crater rim. Plastic flow of material generated micro-notches and micro-cracks that affected fatigue life. For this reason, impacts simulated in quasi-static conditions can provide useful information on the fatigue strength only for low impact speeds, i.e. when the induced microstructural effects are less evident. In contrast, at high speeds, a dynamic model is strictly necessary.

The shape of the crater generated by FOD is influenced by the shape of the impacting particle. For instance, Ding [4] simulated the effects by the impact of a hardened steel cube on a flat specimen in Ti-6Al-4V where the first part that impacted was an edge of the cube. The crater should ideally have a V shape. However, Scanning Electron Microscopy showed rounded corners and irregular sides for the indent. It was assumed that these irregularities came from a combination of deformation of the cube and relaxation of Ti-6Al-4V after impact.

Loss of material (LOM) can be associated with FOD. Experiments show that in the presence of LOM fatigue strength tends to decrease. Martinez et al. [5] stated that it is not so much LOM itself that determines this effect, but the other effects that are often associated: production of sharp edges, folding, and probably relief of compressive stresses. Furthermore, in [5] it was found that LOM creates sites for the initiation of cracks and the fatigue strength decreases as the impact angle increases from 0° (normal impact to the surface) to 30°.

FOD generates notches that determine local stress concentrations that affects fatigue life. In [6], a model based on a rigid sphere that impacts normally to the edge of a plate was proposed in order to model the normal impact on the leading edge of a turbine blade. The plate had a rectangular cross section and the dimensions of the plate was much greater than its thickness. The material of the specimen was considered elastic perfectly plastic and it was assumed that the plastic pile-up at the crater rim was negligible. Results showed that stress concentration essentially depends on the residual penetration of the sphere. At the crater base, higher static stress concentration factor ($K_t$) was found at higher penetration and this was always greater than 1. Therefore, stress concentration plays an important role in the initiation of cracks under cyclic loading. On the other hand, at the bulge tip $K_t$ decreased and was surprisingly always less than 1. This was attributed to the lateral expansion of the material, which is responsible for stress relieving. Therefore, it can be stated that the hypothetical initiation of cracks at the bulge tip is not driven by stress concentration.

Frankel [7] illustrated that FE models tend to overestimate stresses. The reasons for this can be: (i) lack of failure mechanisms, such as initiation of microcracks and formation of shear bands; (ii) scarce consideration of creep effects at room temperature, which can reduce the stresses deriving from the impact; (iii) use of extrapolated and un-validated mechanical properties (experimental data of properties at high strain rate are difficult to find in the literature). In [8], the residual stress distribution obtained with FE modeling for the impact of a steel sphere against a Ti-6Al-4V plate was presented. The distribution of the circumferential residual stresses near the crater was characterized by a large central compression region immediately below the impact crater, two small and intense lateral tensile regions on the crater rim, and two large and intense regions at a distance of about once the radius of the crater. As known, the introduction of residual stresses can positively influence fatigue strength. Ding et al. [4] investigated the influence of FOD-induced residual stresses on Ti-6Al-4V plates by comparing the results obtained for specimens subjected to FOD with those obtained for specimens subjected to FOD and Stress Relief (SR). Under the same load conditions, the fatigue strength for FOD + SR specimens was found to be lower than that of FOD specimens. The residual compressive stresses induced under the crater inhibited the propagation of cracks in that region. However, Ruschau [9] also studied the combined effect of residual stress from FOD and SR. The results showed that SR has substantially no effect in the case of collisions with 2 mm spheres launched at 305 m/s. The huge energy exchange during the impact tends to induce fractures on the specimen causing LOM rather than plastic deformation. Therefore, the residual stress state is small. In contrast, tensile stresses induced by impacts of smaller spheres (diameter of 0.5 mm) were removed by a subsequent SR, with an increase in fatigue strength.

The analysis of the literature highlights the scarce presence of FOD studies on materials other than titanium alloys and on geometries other than plane ones. Aluminum alloy 7075-T6 is widespread in aeronautical and aerospace applications, for components which can be damaged by impact. Fatigue properties of this aluminum alloy with and without coatings in several environments are described in [10-12]. In [10] the fatigue strength of 7075-T6 with and without a diamond-like carbon coating applied by physical vapor deposition in air environment was presented. In [11-12] the corrosion fatigue behavior of 7075-T6 coated with WC/C was studied. In general, coatings increase the wear and corrosion resistance of the components and for this reason their applications on different substrates are studied. For example, in [13] the fatigue strength of steel coated by plasma-enhanced chemical vapor deposition coatings was investigated.

The purpose of this work is to develop a FE model that describes the damage induced by FOD and its consequences on fatigue. The model was applied to the impact of a steel sphere at the minimum cross section of an hourglass specimen in 7075-T6. The cases of normal impact and oblique impact were

studied. The superposition of the residual stresses induced by FOD with the bending stresses made it possible to identify the areas subjected to the highest tensile stresses, which are unfavorable from a fatigue point of view.

## 2. Materials and Methods

Explicit integration method is recommended for FE analyzes involving these types of problems [14-17]. The model was created in Abaqus 2019 and included an hourglass specimen in aluminum alloy 7075-T6 and a steel sphere. The geometries of the components, the mesh and the boundary conditions are shown in Figure 1. The specimen was modelled with 92160 linear hexahedral elements of type C3D8R and an elastic perfectly plastic material. The mechanical properties are: density $\rho$ of 2810 kg/m$^3$, Young's modulus E of 71700 MPa, Poisson's ratio $\nu$ of 0.33, yield stress $R_s$ of 598 MPa. The sphere was modeled with 1536 linear quadrilateral rigid elements of type R3D4. The mass and the moments of inertia were then assigned to the Reference Point (RP) of the sphere, positioned at its center, considering a density of 7860 kg/m$^3$ for steel. The FE model refers to a test rig developed by the authors' research group, which will be used for the experimental validation. The lower left corner of Figure 1 illustrates the specimen support of the rig. The specimen is positioned in the support, with the two cylindrical parts housed in the through holes and is subsequently tightened with set screws. The sphere was considered to be fired by a compressed air-gun setup, which was positioned very close to the firing position. Due to the experimental configuration, the model neglected the contribution of air. The sphere was positioned near the impact zone, in correspondence with the minimum cross section of the specimen, with a gap of 0.1 mm, in order to save on time calculation. Two types of impact were simulated. The first one is normal, i.e. with the impact direction coinciding with the z axis of the coordinate system visible in Figure 1. The second one is oblique, with the impact direction lying on the yz plane. The coefficient of friction implemented between the sphere and the specimen was 0.6. The impact speed was 100 m/s and was defined as a predefined field. The boundary conditions are based on the described specimen support of the test rig. They constraint all the displacements of the nodes on the external surface of the specimen in correspondence with the holes. Symmetry conditions were implemented, consistent with the type of impact analyzed. In detail, the condition of symmetry was set on the plane containing the minimum cross section of the specimen, both in the case of normal impact and in the case of oblique impact. The symmetry condition on the xz plane was only implemented in the case of normal collision. The RP of the sphere was only allowed to translate in the z direction in the case of normal impact and to translate in y and z and rotate around x in the case of oblique impact. An explicit dynamic step of 7 ms was implemented. At the end of the simulation the stresses in the specimen can indeed be considered stabilized. The calculation was performed on four processors.

## 3. Results and discussion

Normal and oblique impacts were studied. Results were analyzed firstly in terms of contact elastic and residual stresses induced by the impact of the sphere with the specimen. Secondly, the effects of rotating bending experiment were included in the impact model in order to discuss fatigue implication of the impact. The units of measurement adopted for the analyses are mm for lengths, kg for masses and ms for times. For this reason, stresses and pressures are in GPa.
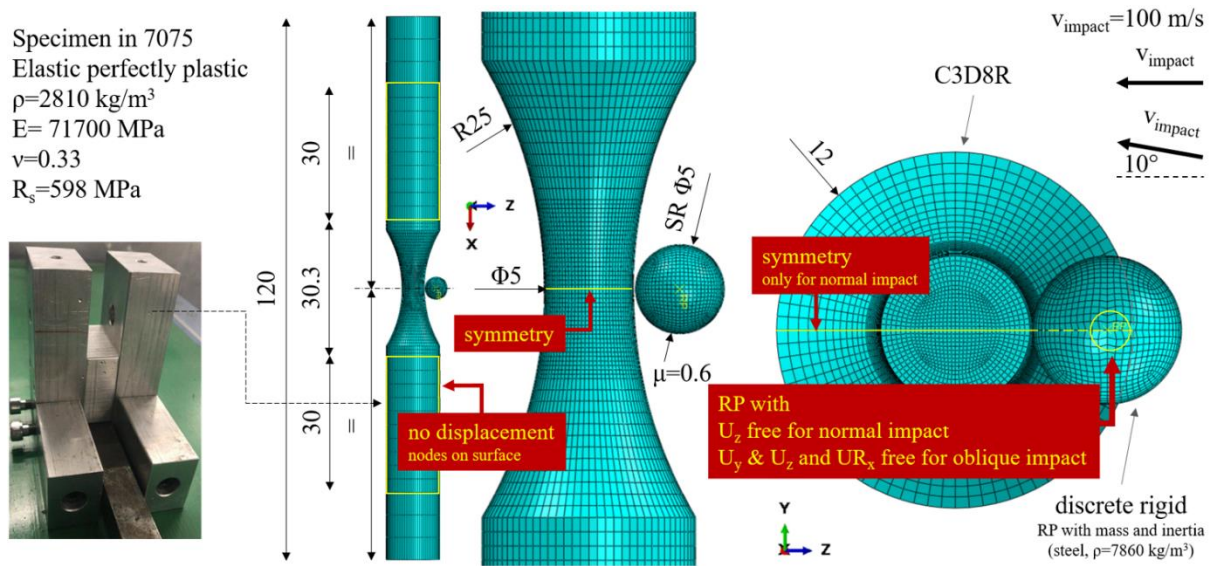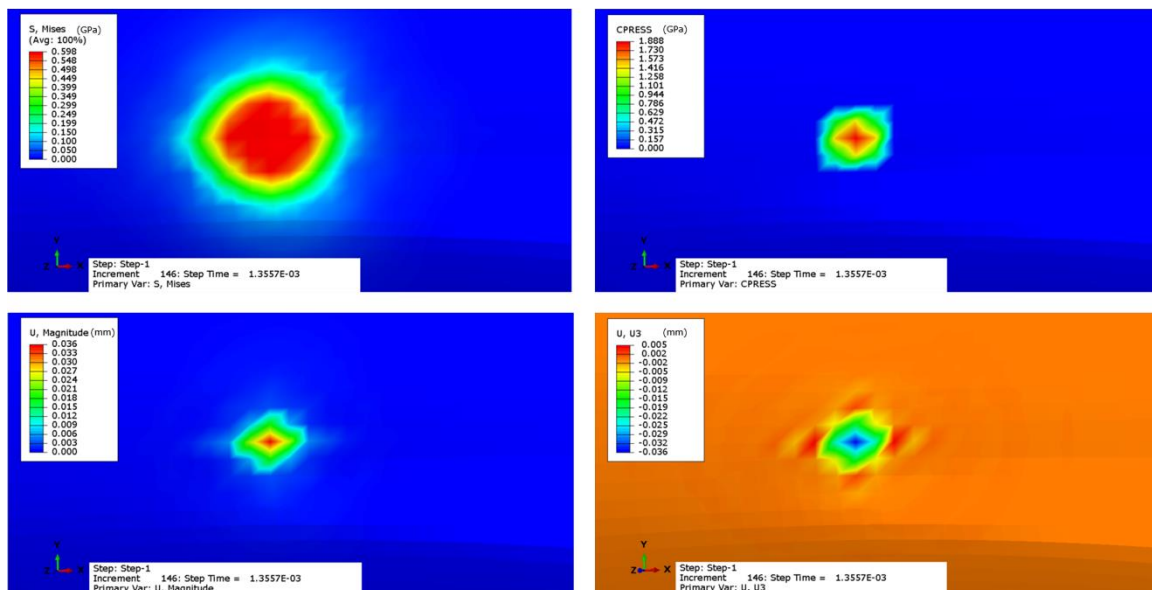
**Figure 1.** FE model.

Contact stresses and displacements are illustrated in Figure 2. This shows the von Mises stress, the contact pressure, the total displacement and the displacement in impact direction (z). Stresses, pressure and displacement distributions refer to 0.00136 ms after the start of motion of the sphere. At this point of the impact process, the specimen is in the proximity of the yielding of the specimen material. Thus, these distributions are substantially elastic. The von Mises stress and the contact pressure exhibit a maximum value at the center of the contact area and decrease to edge. The stress state shows the typical distribution by application of a surface pressure distribution, e.g. Hertzian. Displacement distribution is analogous to the stress one, with the maximum value in magnitude reached at the center of the contact area. By comparison of displacement magnitude and displacement in impact direction, it can be observed that the displacement at the center of the contact area is only in z direction. This result is coherent with the symmetry of the analyzed problem.



**Figure 2.** Normal impact: von Mises, contact pressure, displacement and displacement in z.

The residual stresses and the displacements in the minimum cross section obtained with the normal impact are shown in Figure 3. Particularly, S11, S22, S33 are the stresses in the x, y, z directions while S23 is the shear stress on yz plane, the other shear stresses are not reported because they are negligible. The von Mises equivalent stress is S, Mises while U indicates the magnitude of the total displacement. Arrows indicates the impact direction. In proximity of contact surfaces, there are only normal stress similarly to general solution of elastic stresses state originated by contact pressure distribution [18].

**Figure 3.** Normal impact: S11, S22, S33, S23, von Mises, displacement.

The S11 contour in Figure 3 shows that, in proximity of the crater, only a small region near the rim exhibits moderate tensile stresses in axial direction while the maximum axial stress can be found in surface regions between the rim and the vertical radius, corresponding approximately to the angular positions $9.0° \leq \theta \leq 45.0°$. The angle $\theta$ was measured starting from the vertical direction, which is normal

to the impact direction, i.e. from the y direction. It was positive in counterclockwise direction and measured from the top of the section, which corresponds to the maximum y. This stress distribution is coherent with the result found by Boyce et al. [8]. Assuming that the specimen is subject to a post impact fatigue test based on rotating bending, a further stress distribution in axial direction has to be considered in order to assess the final stress state during the test. Therefore, the typical axial stress distribution of the rotating bending was added to the residual stresses induced by FOD. Due to the rotation, the constant bending stress distribution will be applied to each point of the cross section. The region with the highest tensile stresses state might have a higher probability of cracks initiation. Considering that bending stresses applied by fatigue test are constant over time, the maximum tensile stress will be reached when the maximum residual stress overlaps the maximum tensile stress generated by the test. In order to better identify this region, Figures 4 and 5 report the trends of the axial residual stresses after the normal impact at the different angular positions. Particularly, Figure 4 refers to the axial stresses for the angular positions $9.0° \leq \theta \leq 45.0°$ while Figures 5 displays the axial stresses at $\theta = 0°$ and $\theta = 90°$ and in the direction that passes through the center of the cross section and the bulge tip ($\theta = 67.5°$). The last point is very important because the maximum tangential displacement occurs near this point [19-21]. The reason is that the contact pressure is zero and therefore, for any coefficient of friction, displacement is possible. The stresses were plotted on a stress – $r_{final}/r$ diagram, where $r_{final}$ is the radial coordinate on the deformed section and r is the radius of the undeformed minimum cross section. In the diagram, various angular positions are plotted. This diagram is also useful for appreciating the deformation of the section. Radial expansions correspond to values of $r_{final}/r$ higher than 1. In Figure 4, the residual axial stresses are plotted only for the annulus in proximity of the surface.
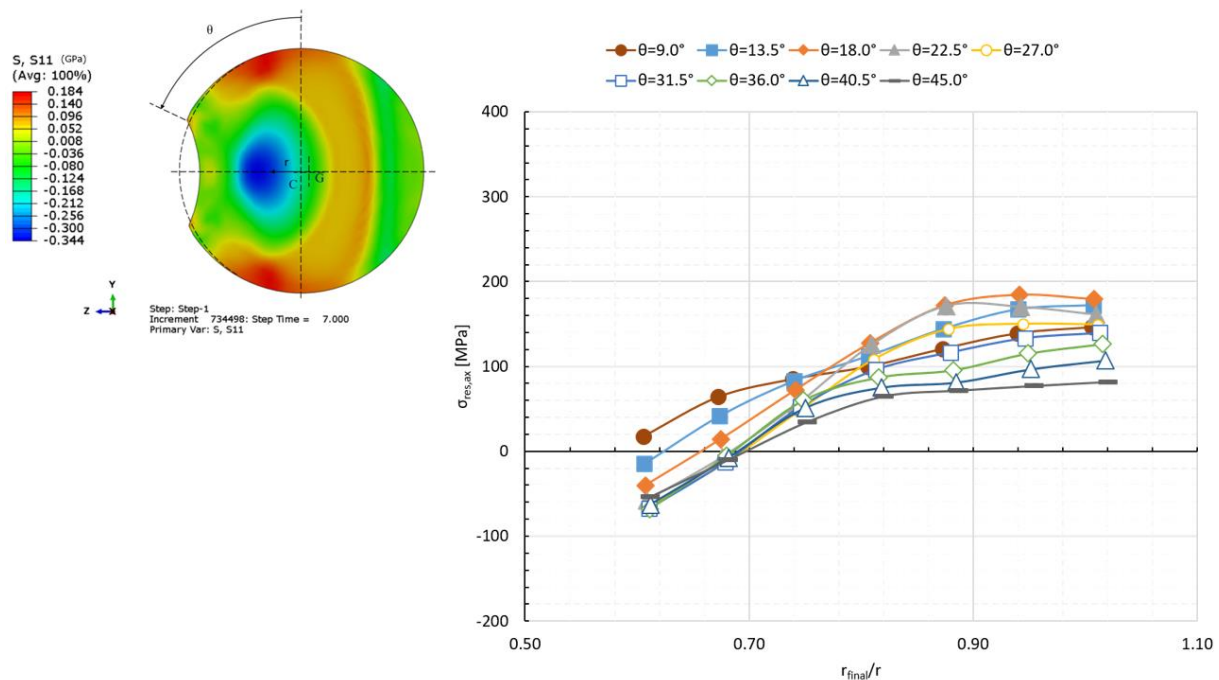


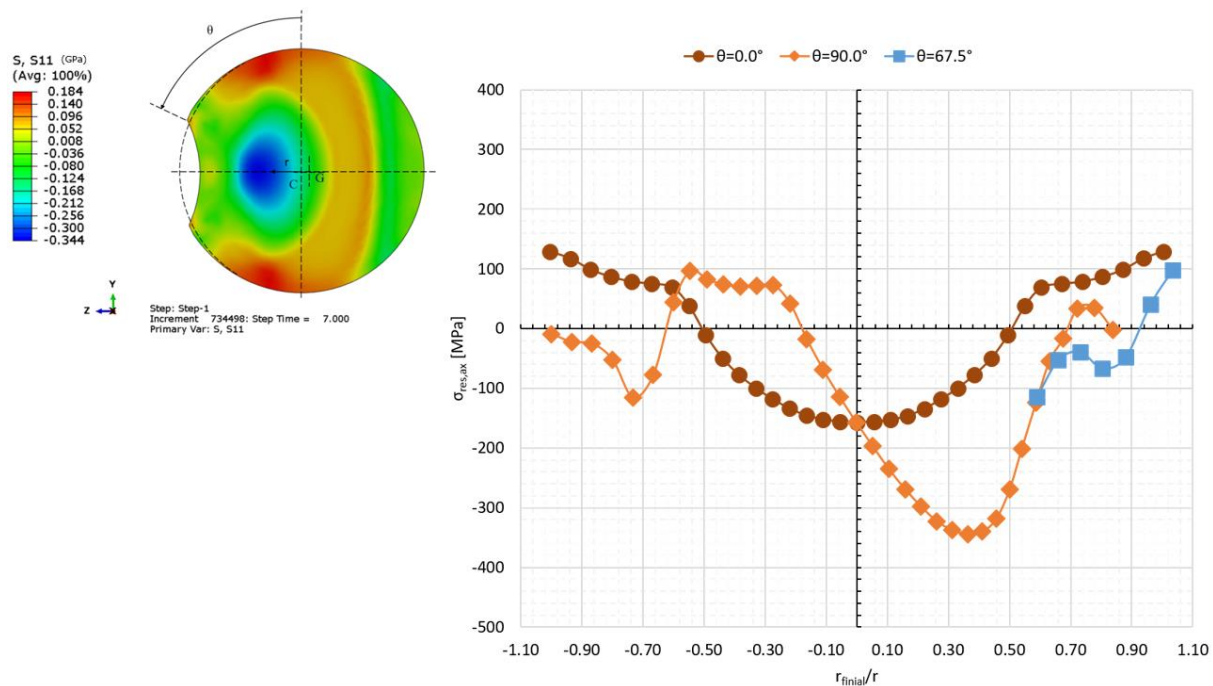**Figure 4.** Normal impact: axial residual stresses, $9.0° \leq \theta \leq 45.0°$.

**Figure 5.** Normal impact: axial residual stresses, θ=0.0°, 67.5°, 90.0°.

In order to analyze the stresses during rotating bending fatigue test, the residual axial stresses induced by the normal impact (Figures 4 and 5) were superposed with the bending stresses in the minimum specimen cross section. The bending stresses added to the residual stresses were obtained by the application of a moment of 1.5 Nm. The magnitude of the applied bending moment was estimated according to the results of previous experiments for determining the fatigue strength of smooth hourglass specimens in 7075-T6 [22-24]. The bending stresses were added and subtracted to the residual stresses in order to identify the maximum and minimum total axial stresses experienced by all the points of the considered direction during the fatigue test. Figure 6 shows the results of the stress superposition of bending stresses to the stresses plotted in Figure 4, 9.0°≤θ≤45.0°. To increase in readability of the figure, only the stresses for the angular positions which provide the highest maximum stresses are plotted. The axial tensile stresses reach a maximum value of about 180 MPa at 13.5°≤θ≤22.5°. The maximum total tensile stress is about 300 MPa and it is included in the angular region between θ=13.5° and θ=18.0°.

In Figure 7, residual and fatigue stresses were superimposed on the specific directions reported in Figure 5. This figure provides a global vision. The total axial tensile stresses reach a maximum value of around 250 MPa on the vertical radius and of around 240 MPa at θ=67.5°. For this reason, it can be expected that the fatigue cracks nucleate in the region corresponding between θ=13.5° and θ=18.0° of the minimum cross section if the defects are uniformly distributed in the specimen. However, the relative displacements at the crater rim might induce there a crack nucleation [19-21].
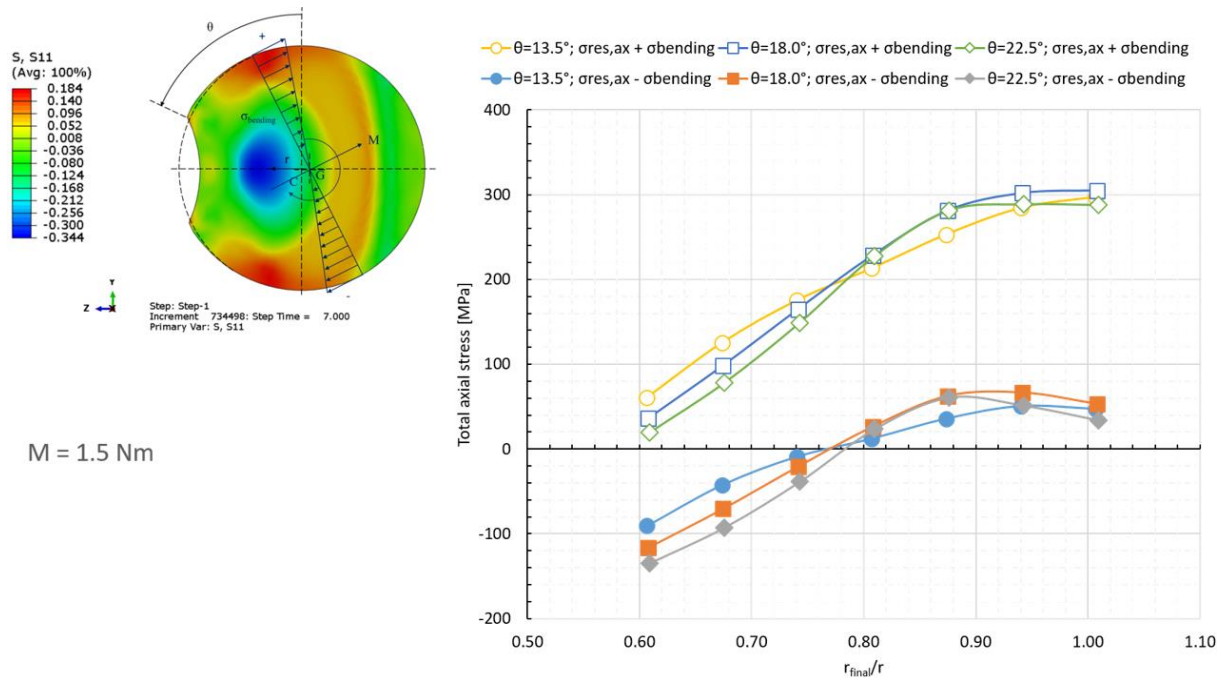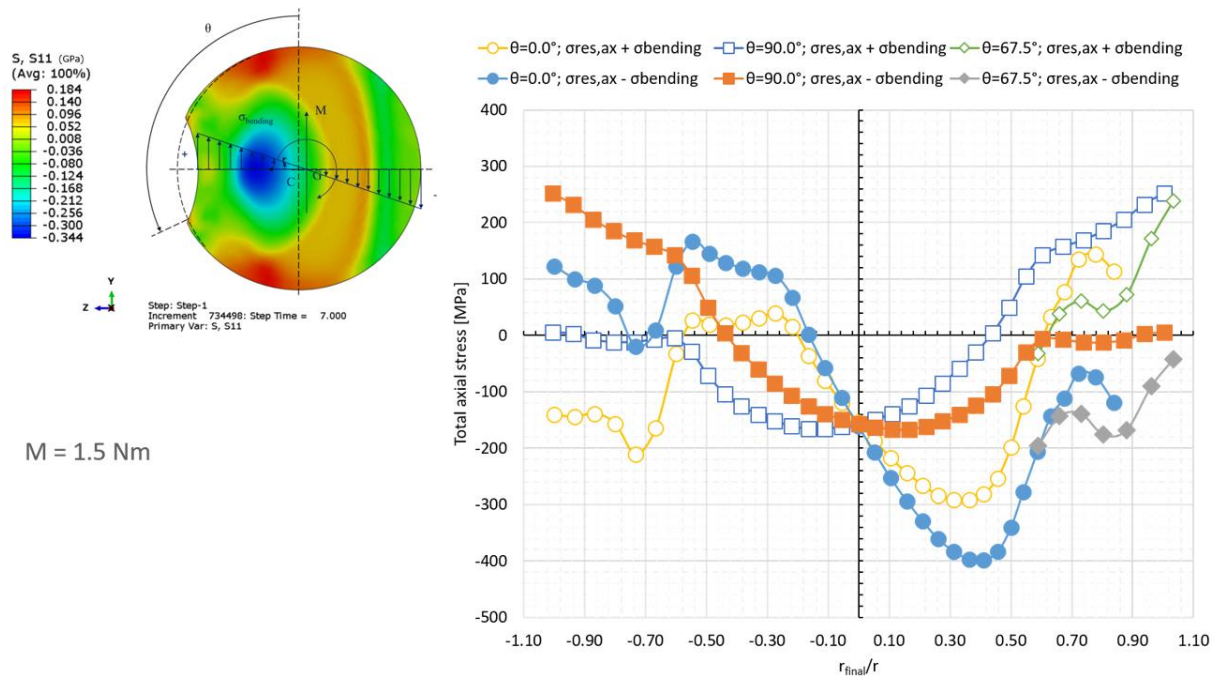
**Figure 6.** Normal impact: total stresses, 13.5°≤θ≤22.5°.



**Figure 7.** Normal impact: total stresses, θ=0.0°, 67.5°, 90.0°.

The same method was applied to determine the total stresses induced by the oblique impact. Figure 8 shows the von Mises stress, the contact pressure, the total displacement and the displacement in z direction. The shown fields refer to 0.00145 ms after the start of motion of the sphere, in the proximity of the yielding of the specimen material. Therefore, the analyzed distributions are substantively elastic. The obtained distributions are symmetric with respect to yz plane but they are not symmetric with respect to xz. The asymmetry is clearly visible in the von Mises stress distribution, which shows a larger

light blue are at the top. The maximum values of equivalent stresses are reached near the center of the contact area, because of the small impact angle. By comparison of displacement magnitude and displacement in z direction, it can be observed that the maximum displacement is not only in z direction like in normal impact. In oblique impact, the displacement presents two components, one z-oriented and the other one y-oriented. All these results are coherent with the direction of impact.
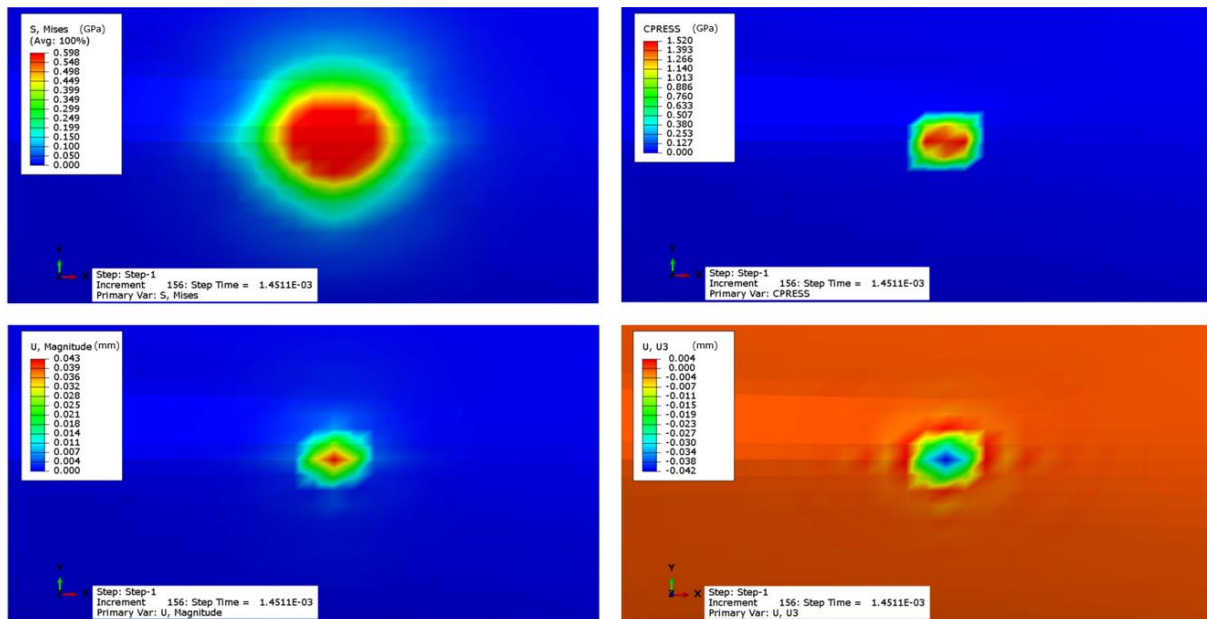


**Figure 8.** Oblique impact: von Mises, contact pressure, displacement and displacement in z.

Figure 9 shows the stresses and the displacements in the minimum cross section obtained with the oblique impact. In detail, S11, S22, S33, S23, von Mises stress and the total displacement are shown. The other shear components are not shown because they are negligible similarly to the normal impact case. Substantially there is no shear in proximity of contact surfaces. Therefore, the stress state is determined only by normal stress similarly to general solution of elastic stresses state originated by contact pressure distribution [18]. Figure 9 shows that the stress and displacement distributions are not symmetric with respect to xz plane and the maximum stresses are reached in the upper part of the specimen, where the sphere speed is directed. The region in the upper part of the specimen is more stressed in oblique impact than in normal. The maximum stress region in oblique impact is located closer to the crater. According to Figure 9, the point of the crater rim in the lower part of the section ($\theta$=112.5°) is more stressed than the upper one. Figures 10 shows the stress trends at 9.0°$\leq\theta\leq$45.0°. At these angular positions, the highest axial stresses induced by FOD were found. This region (red in Figure 9) is located between the rim and the vertical radius. Figure 11 shows the trends at $\theta$=0°, 90° and 112.5°. At this point, the maximum residual axial stress is about 200 MPa at 27.5°$\leq\theta\leq$40.5°, Figure 10. The maximum axial stress induced by the oblique impact is higher than in normal impact, which was about 180 MPa. The stresses at the lower crater rim are higher in oblique (about 150 MPa, Figure 11) than in normal impact (about 100 MPa, Figure 5).
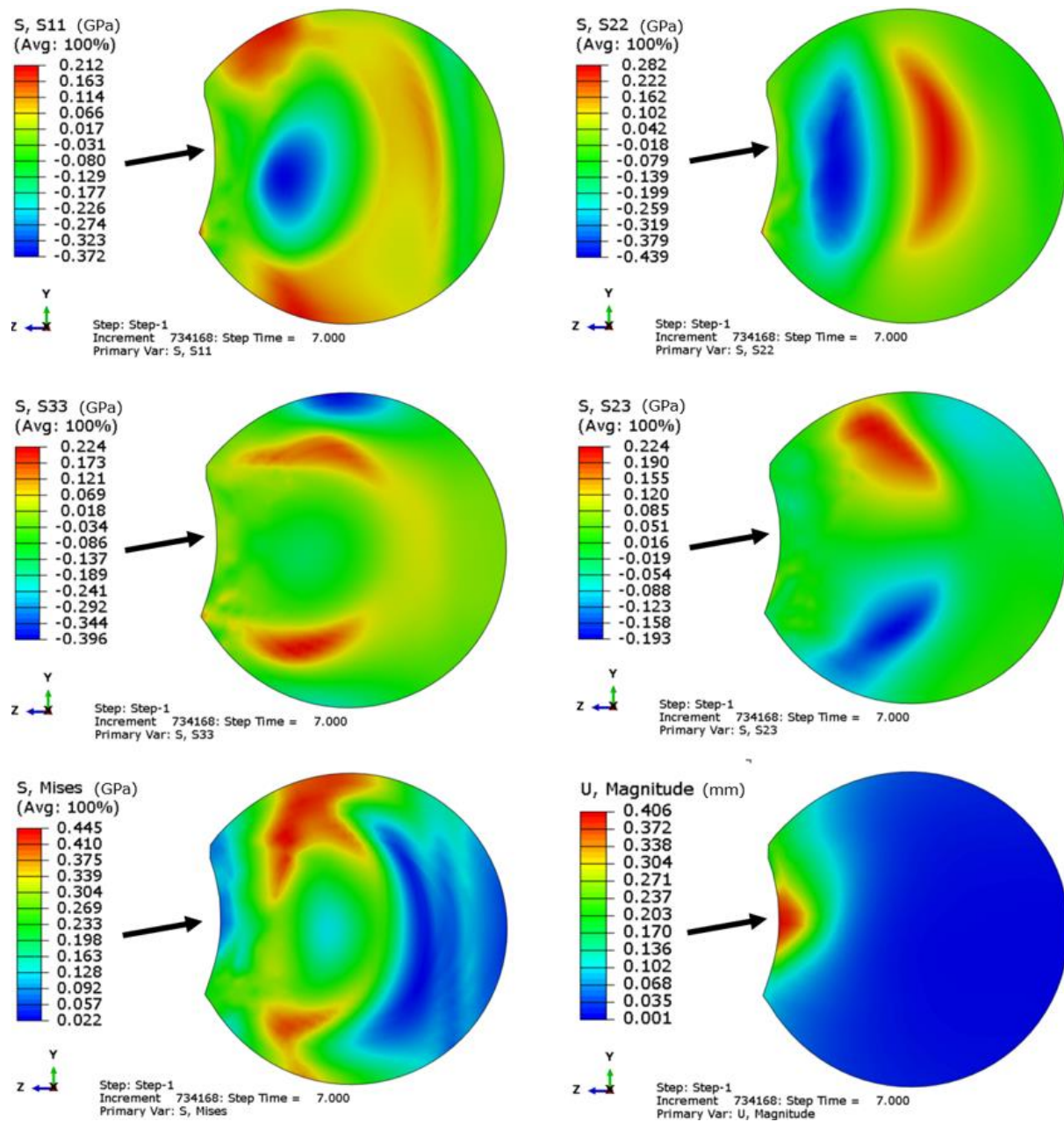
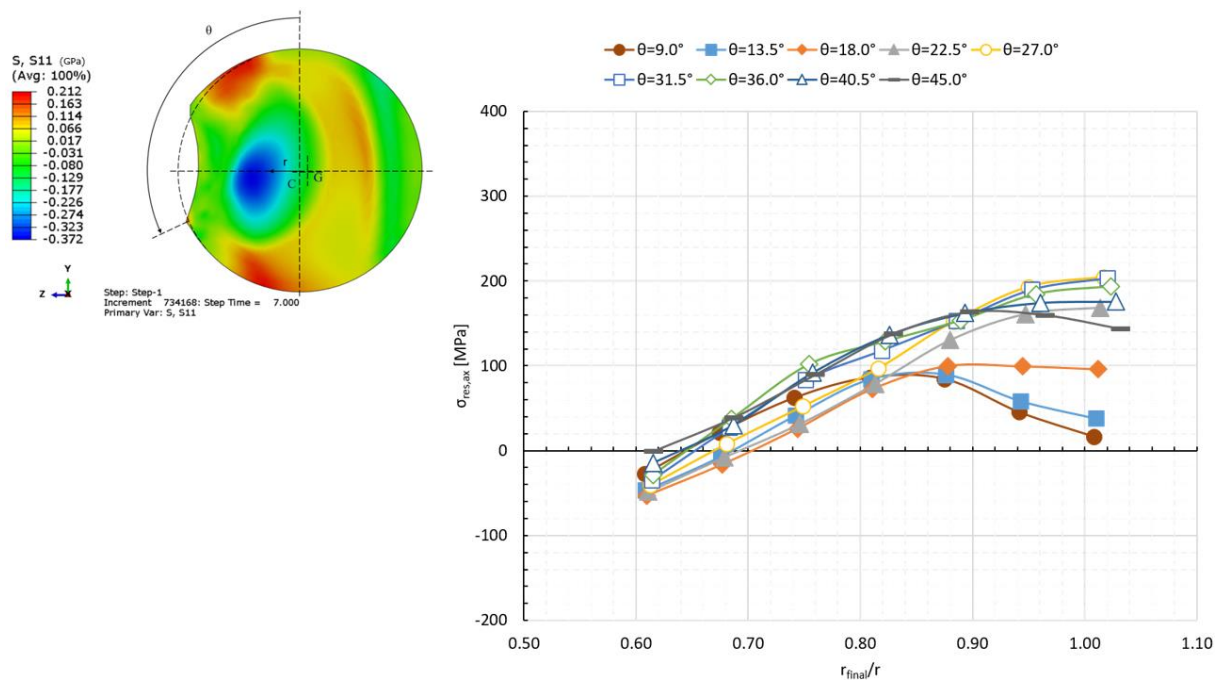**Figure 9.** Oblique impact: S11, S22, S33, S23, von Mises, displacement.

**Figure 10.** Oblique impact: axial residual stresses, 9.0°≤θ≤45.0°.



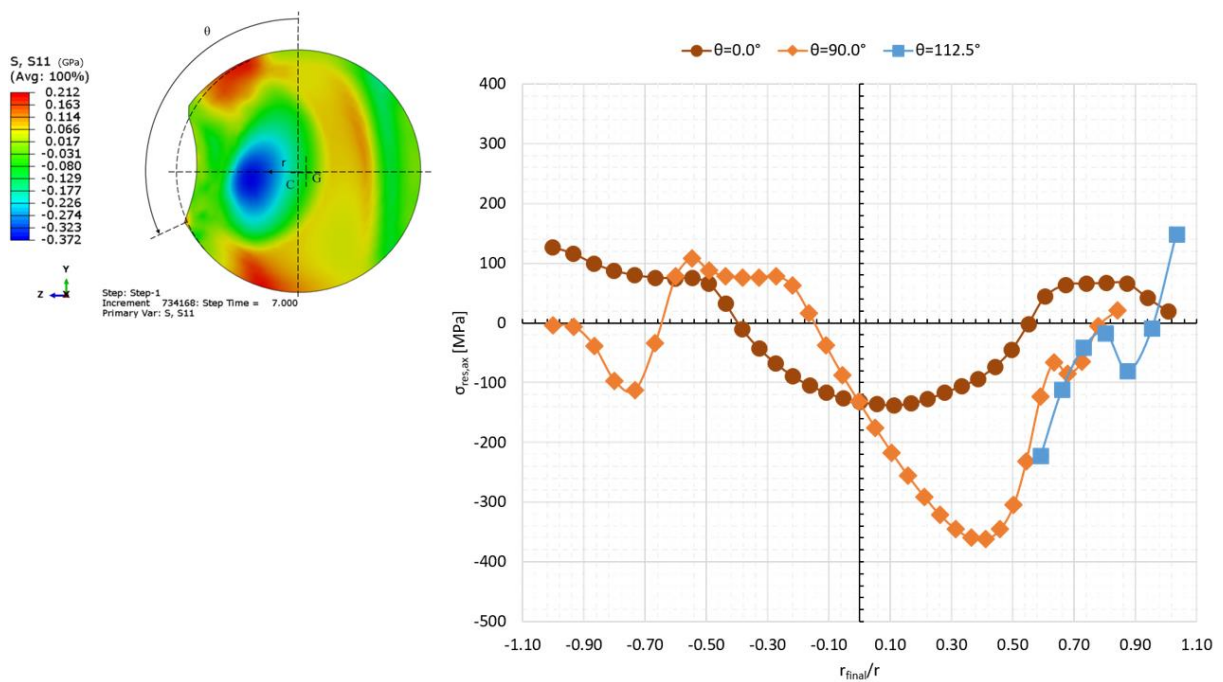**Figure 11.** Oblique impact: axial residual stresses, θ=0.0°, 90.0°, 112.5°.

Figure 12 shows the results of the stress superposition of the bending stresses to the residual stresses of Figure 10. The maximum axial stress in the minimum cross section over the time in the fatigue test is approximately 330 MPa, with an increment of 30 MPa with respect to the normal impact. The maximum values are reached at 27.0°≤θ≤31.5°. Figure 13 shows the results of the stress superposition

of bending stresses to the residual stresses at three angular positions: θ=0.0°, θ=90.0° and θ=112.5°. The maximum axial stress at the crater rim is about 290 MPa.



**Figure 12.** Oblique impact: total stresses, 27.0°≤θ≤31.5°.



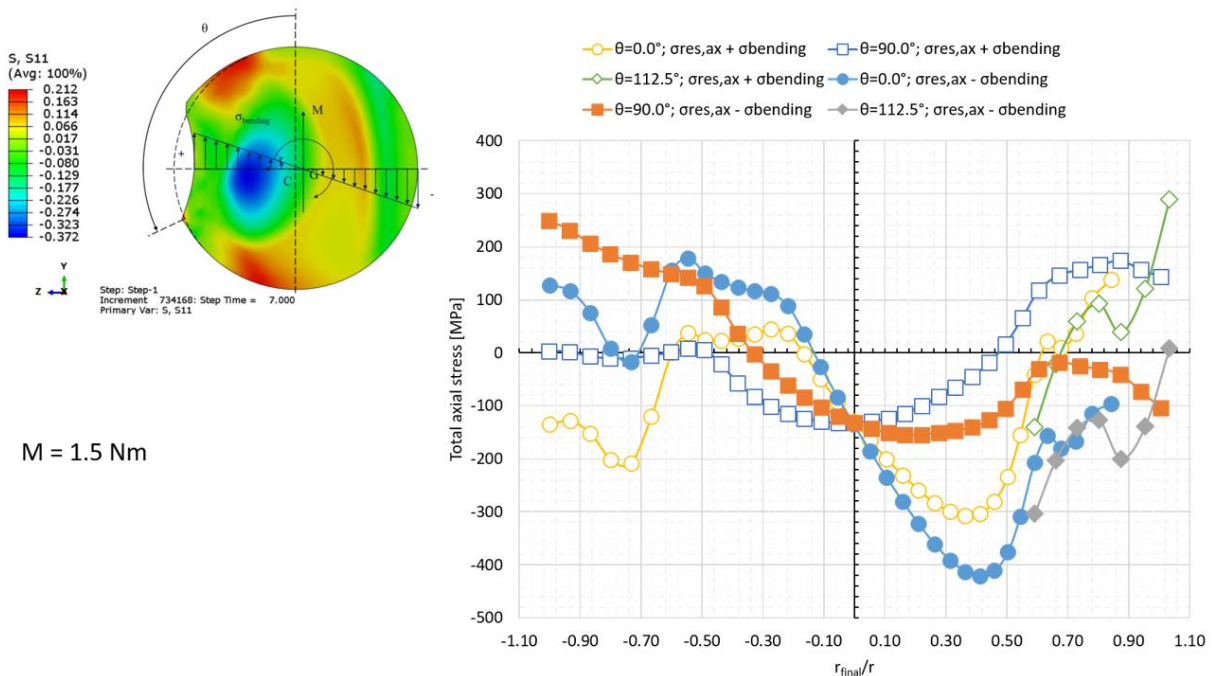**Figure 13.** Oblique impact: total stresses, θ=0.0°, 90.0°, 112.5°.

Therefore, in the case of oblique impact, crack initiation can be expected at an angular position between 27.0° and 31.5°, where the maximum stress of 330 MPa is reached, or at θ=112.5°, i.e. at the

crater rim. Here a maximum stress of 290 MPa can be observed but the relative displacements contribute to crack nucleation.

## 4. Conclusions

A model of FOD by steel sphere on hourglass 7075-T6 specimen was developed in order to evaluate residual stress field effects on fatigue test. The cases of normal and oblique impacts were studied. The stress distributions induced in the minimum cross section were compared. It was found that oblique impact introduces higher axial stresses (tensile). These stresses are closer to the crater generated by the collision. A rotating bending moment was applied to the specimen. The superposition of the FOD-induced stresses to the bending stresses allowed to identify the regions of the minimum cross section which are unfavorable from a fatigue point of view.

## References

[1]     Nicholas T 2006 Foreign Object Damage *High Cycle Fatigue*, Elsevier Science Ltd (Oxford) pp x–xiv
[2]     Lin B, Zabeen S, Tong J, Preuss M and Whiters P J 2015 *Mech. Mater.* **82** 78
[3]     Peters J O and Ritchie RO 2000 *Eng. Fract. Mech.* **67** 193
[4]     Ding J, Hall R F, Byrne J and Tong J 2007 *Int. J. Fatigue* **29** 1339
[5]     Martinez C M, Eylon D, Nicholas T, Thompson S R, Ruschau J J, Birkbeck J and Porter W J 2002 *Mat. Sci. Eng.* **A325** 465
[6]     Chen X 2005 *Mech. Mater.* **37** 447
[7]     Frankel P G, Withers P J, Preuss M, Wang H T, Tong J and Rugg D 2012 *Mech. Mater.* **55** 130
[8]     Boyce B L, Chen X, Hutchinson J W and Ritchie R O 2001 *Mech. Mater.* **33** 44
[9]     Ruschau J, Thompson S R and Nicholas T 2003 *Int. J. Fatigue* **25** 955
[10]   Baragetti S, Borzini E, Bozic Z and Arcieri E V 2019 *Eng. Fail. Anal.* **102** 219
[11]   Baragetti S, Gerosa R and Villa F 2014 *Key Eng. Mater.* **577-578** 221
[12]   Baragetti S, Gerosa R and Villa F 2016 *Eng. Fract. Mech.* **164** 106
[13]   Baragetti S and Tordini F 2007 *Int. J. Fatigue* **29** 1832
[14]   Arcieri E V, Baragetti S, Fustinoni M, Lanzini S and Papalia R 2018 *Procedia Struct. Integrity* **8** 212
[15]   Baragetti S and Arcieri E V 2019 *ASME Int. Mechanical Engineering Congr. and Expo.* vol 14 (Salt Lake City) 156960
[16]   Baragetti S and Arcieri E V 2019 *Procedia Struct. Integrity* **24** 91
[17]   Baragetti S and Arcieri E V 2020 *Eng. Fail. Anal.* **113** 104564
[18]   Johnson K L 1985 *Contact Mechanics* (Cambridge University Press)
[19]   Lavella M 2020 *Tribol. Int.* **146** 106163
[20]   Lavella M and Botto D 2018 *Mater.* **11** 1052
[21]   Botto D and Lavella M 2015 *Wear* **330-331** 629
[22]   Arcieri E V, Baragetti S and Borzini E 2018 *Key Eng. Mater.* **774** 1
[23]   Baragetti S, Bozic Z and Arcieri E V 2020 *Eng. Fail. Anal.* **112** 104512
[24]   Baragetti S and Arcieri E V *P. I. Mech. Eng. C.-J. Mec.* (submitted)